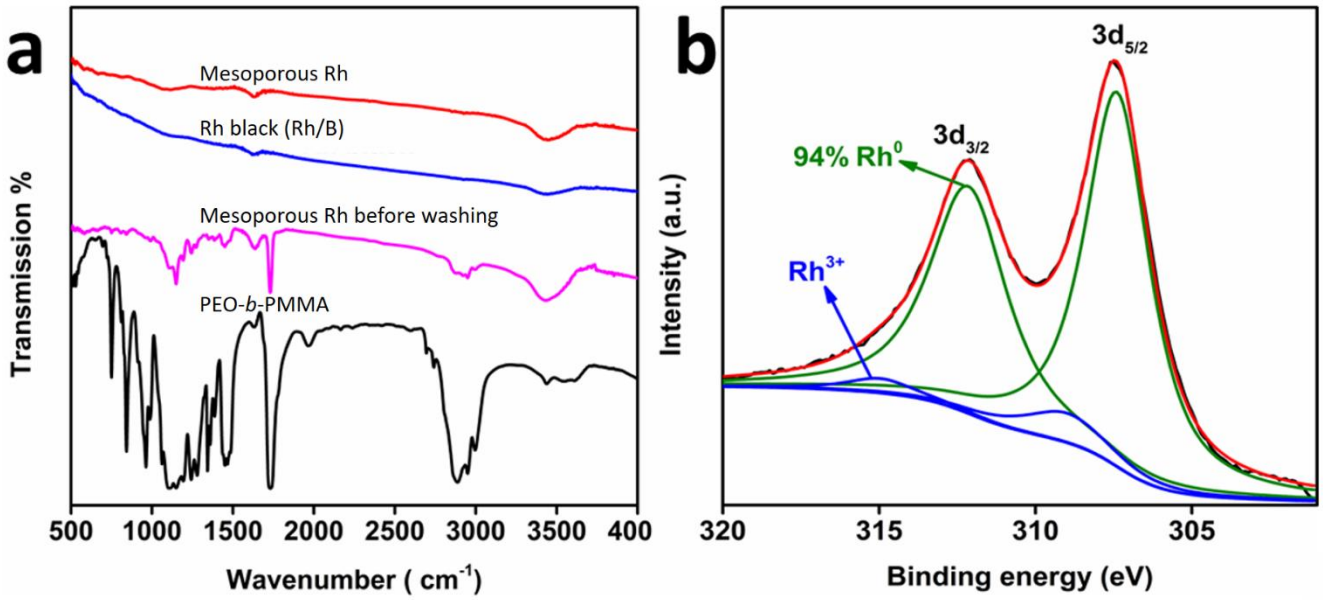


**Supplementary Figure 1. FI-IR spectra and XPS spectrum.** (**a**) FT-IR spectra of the mesoporous Rh nanoparticles before and after the washing procedure. For reference, additional spectra showing commercially available Rh black (Rh/B) and block polymer PEO-*b*-PMMA, respectively. (**b**) XPS spectrum of the mesoporous Rh nanoparticles after the washing procedure.

**Supplementary Note 1:** The IR peaks derived from PEO-*b*-PMMA template disappered after the washing procedure. From CHNSO analysis, the carbon and oxygen contents are < 1-2 wt%, respectively. From the XPS data, most of Rh atoms on the surface are not oxidized in air.

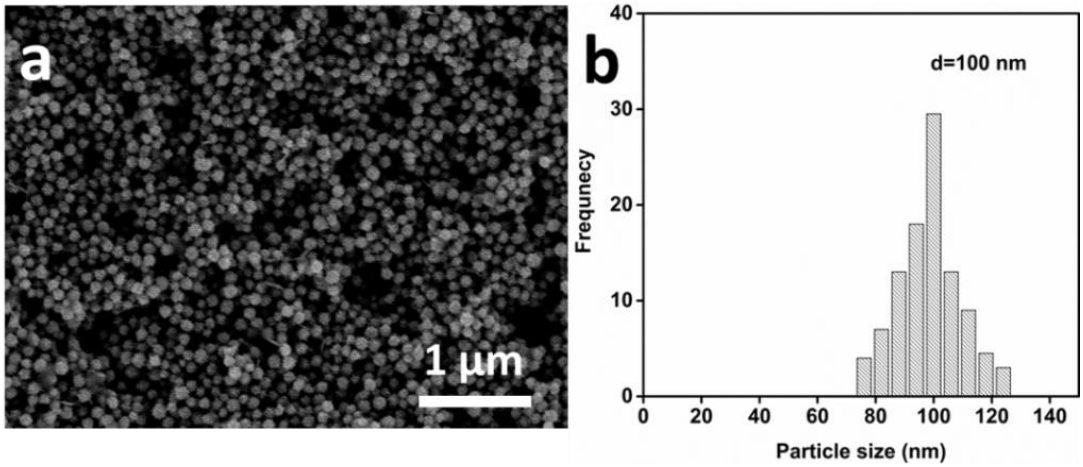


**Supplementary Figure 2. SEM micrograph and histogram showing the particle size distribution.** (**a**) SEM micrograph of the mesoporous Rh nanoparticles at low magnifications. (**b**) A histogram showing the particle size distribution of the mesoporous Rh nanoparticles.

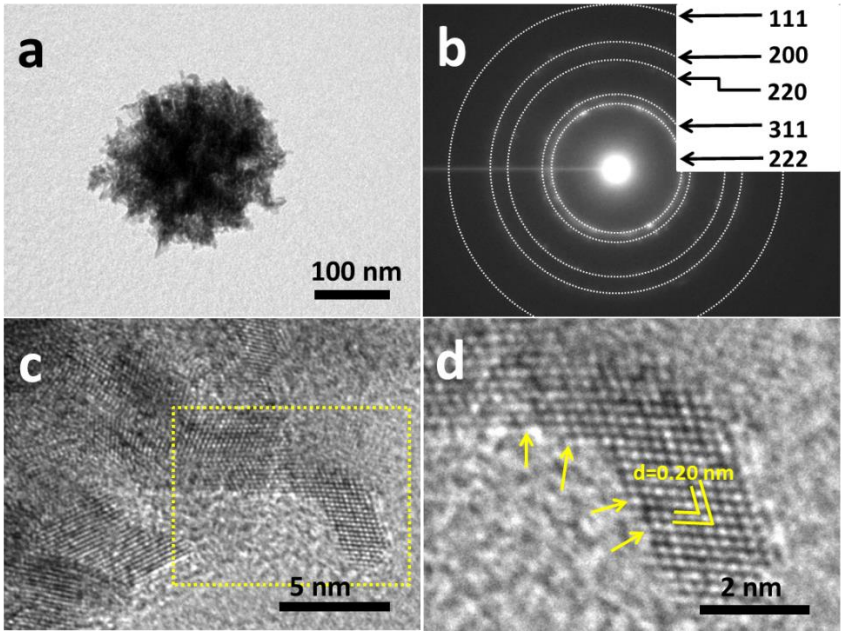


**Supplementary Figure 3. TEM study.** (**a**) TEM image of a single mesoporous Rh nanoparticle, (**b**) the SAED pattern obtained from the single particle, and (**c, d**) HRTEM images of mesoporous Rh nanoparticles. The kink and step sites are indicated by the yellow arrows.

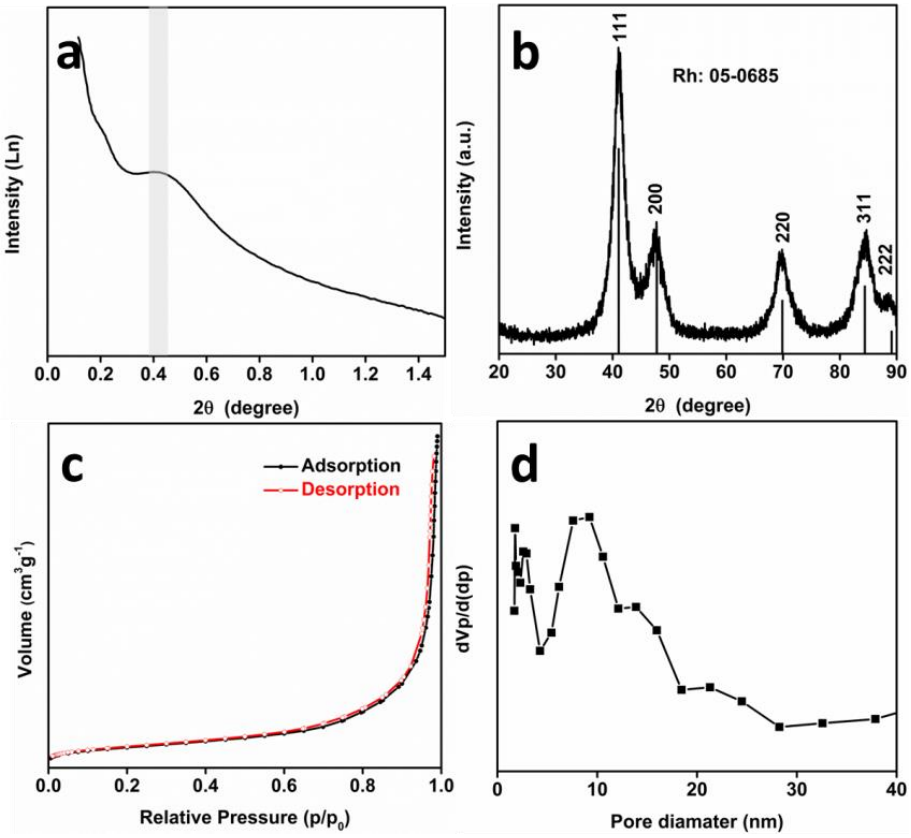


**Supplementary Figure 4. Low-, and wide-angle XRD patterns, $N_2$ adsorption-desorption isotherms, and the BJH pore size distribution curve.** (**a**) Low-, and (**b**) wide-angle XRD patterns of mesoporous Rh nanoparticles. (**c**) $N_2$ adsorption-desorption isotherms and (**d**) the BJH pore size distribution curve of mesoporous Rh nanoparticles.

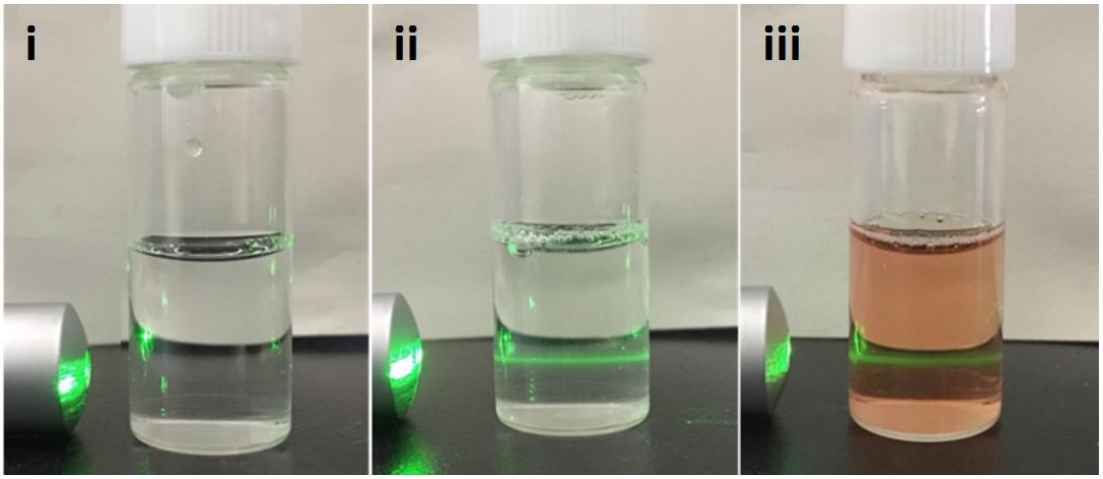


**Supplementary Figure 5. Optical micrographs.** Optical micrographs demonstrating the emergence of the Tyndall effect in the electrolyte solution with different composition: (i) PEO-*b*-PMMA dissolved in DMF, (ii) PEO-*b*-PMMA dissolved in DMF+water, and (iii) PEO-*b*-PMMA dissolved in DMF+water+$Na_3RhCl_6$.

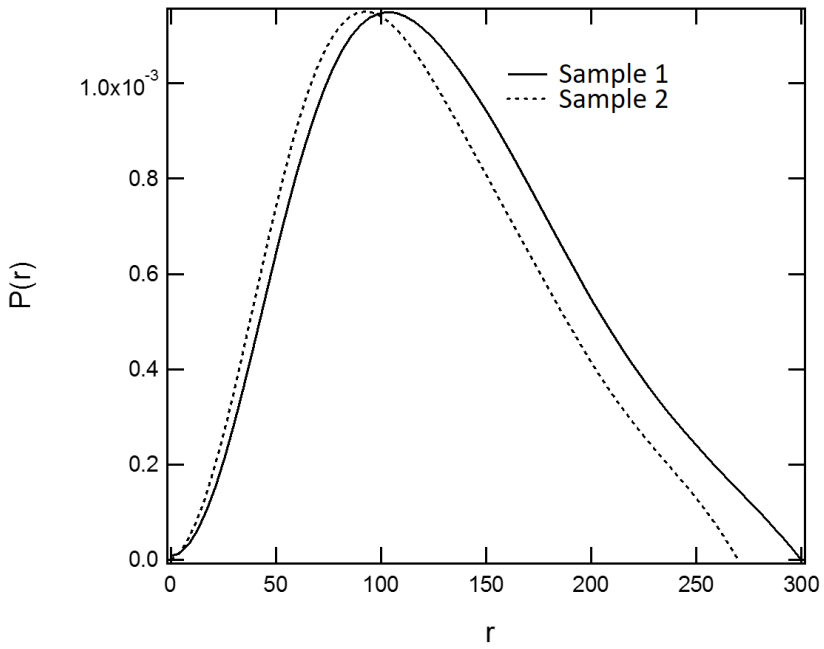


**Supplementary Figure 6. Radial probability distribution function extracted from the small angle neutron scattering data.** Sample 1 solution was prepared by mixing 5 mg of PEO-*b*-PMMA, 0.6 mL of DMF, 1 mL of 40 mM $Na_3RhCl_6$ solution in $H_2O$, and 1.4 mL $D_2O$, while Sample 2 was prepared by mixing 5 mg of PEO-*b*-PMMA, 0.6 mL of DMF, and 1 mL of 40 mM $Na_3RhCl_6$ solution.

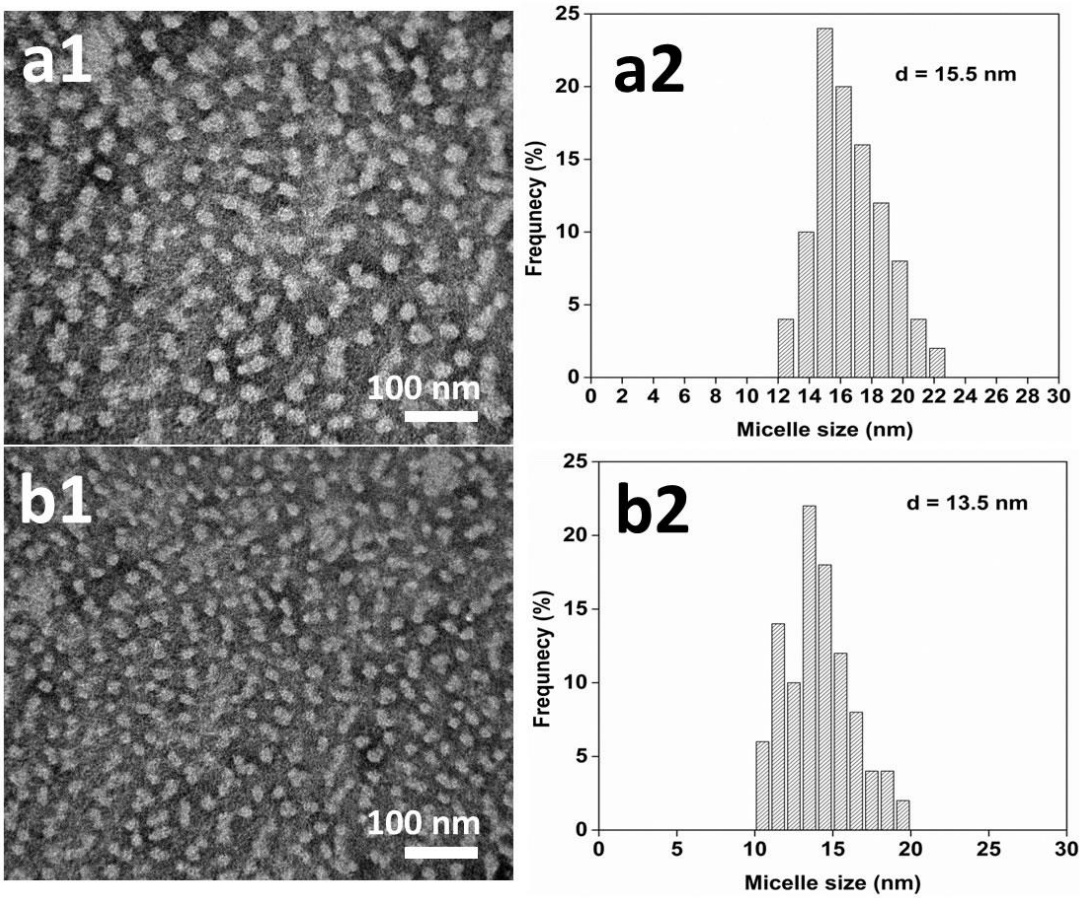


**Supplementary Figure 7. SEM micrograph and histogram showing the micelle size distribution.** Low-magnification TEM micrographs and histogram showing the size distribution of the polymeric micelles (a) before and (b) after the addition of $Na_3RhCl_6$. To highlight the micelle structures, the samples were stained with 1.0 wt% phosphotungstic acid.

**Supplementary Note 2:** Previous report has described the effect of $Cl^-$, $Br^-$, and $I^-$ on micellization and the subsequent effect on mesoporous silica (*Langmuir*, **2011**, 27, 7121-7131)). In this series, $Cl^-$ is a hydrotropic ion and that enhances micellization, while the $I^-$ ion is lyotropic and inhibits micellization. The role of hydrotropic anions is structural and somehow effects the aqueous assembly of surfactants into micelles with a smaller corona. The TEM micrographs in **Supplementary Figure 7** also support this conclusion that the micelles become quantitatively smaller upon addition of the Rh salt into the media. It is likely that either $[RhCl_{6-x}(H_2O)]^{(3-x)-}$ precursor or $Cl^-$ ions released into solution due to ligand exchange, enhance micellization. This results in increasingly compact micelles during the further assembly process.

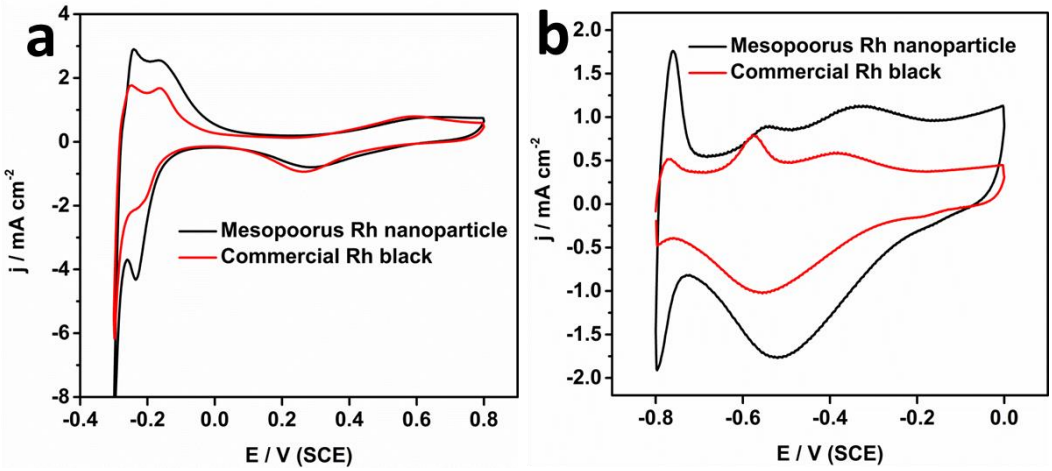


**Supplementary Figure 8. Cyclic voltammogram (CV) curves.** Cyclic voltammogram (CV) curves of the mesoporous Rh and commercial Rh black in $N_2$-purged (a) 0.5 M $H_2SO_4$ solution, and (b) 1 M KOH at 50 $mV \cdot s^{-1}$.

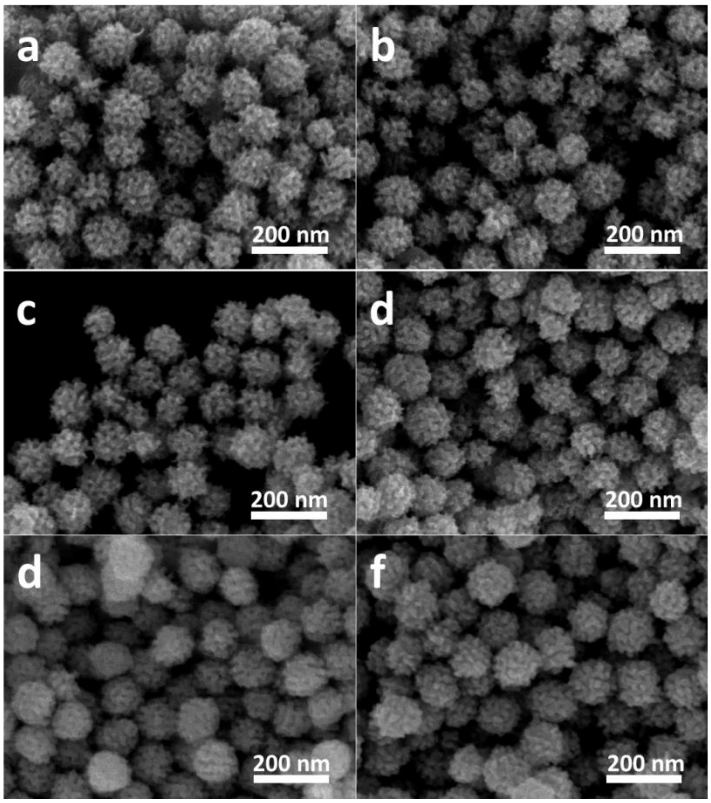


**Supplementary Figure 9. SEM micrographs.** SEM micrographs of mesoporous Rh nanoparticles after thermal treatment at different temperatures: (a) 250 $^{o}$C, (b) 300 $^{o}$C, (c) 350 $^{o}$C, (d) 400 $^{o}$C, (e) 450 $^{o}$C and (f) 500 $^{o}$C in air atmosphere.

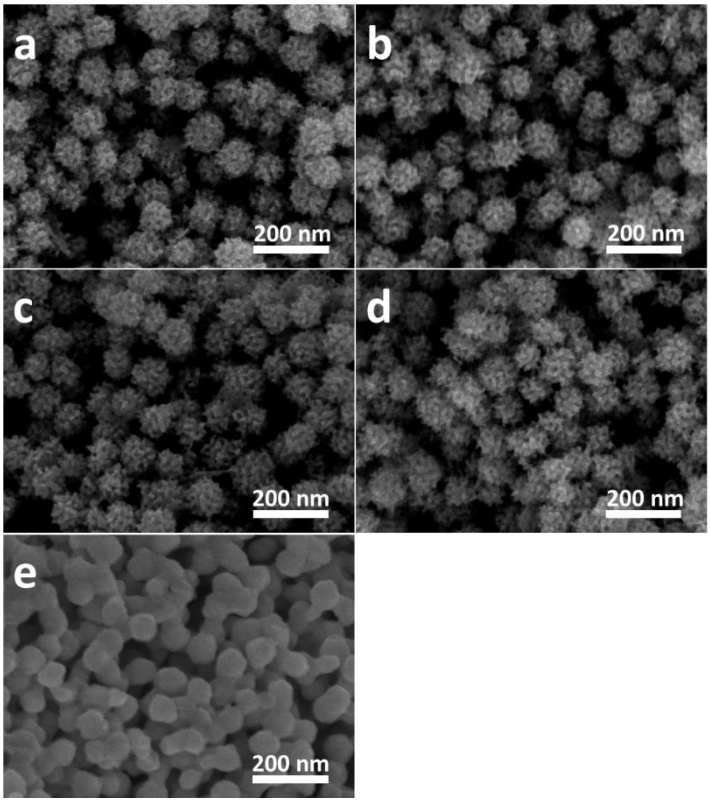


**Supplementary Figure 10. SEM micrographs.** SEM micrographs of mesoporous Rh nanoparticles after thermal treatment at different temperatures: (a) 250 $^{o}$C, (b) 300 $^{o}$C, (c) 350 $^{o}$C, (d) 400 $^{o}$C, and (e) 450 $^{o}$C in nitrogen atmosphere.

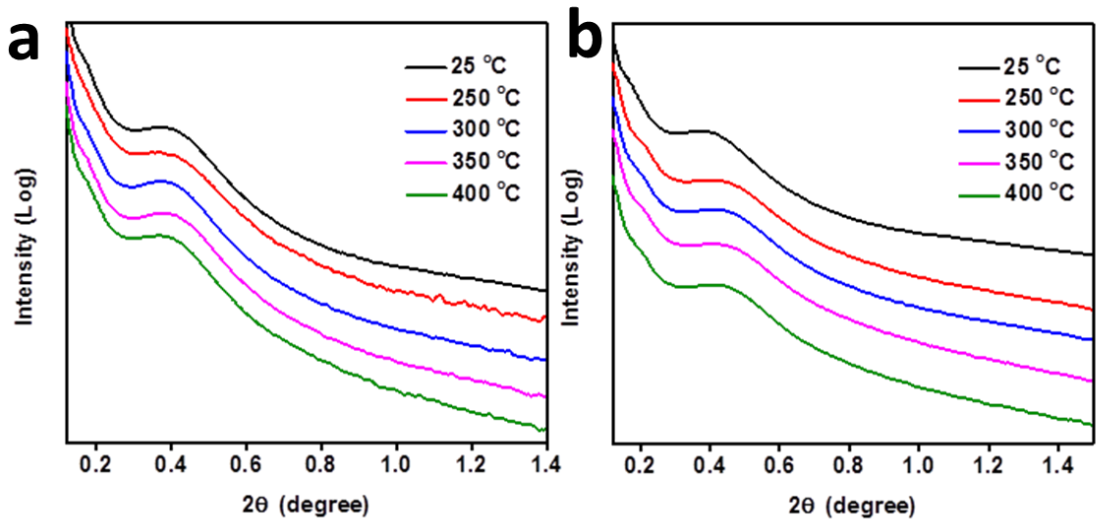


**Supplementary Figure 11. Low-angle XRD patterns.** Low-angle XRD patterns of mesoporous Rh nanoparticles after thermal treatment at different temperatures (25 °C, 250 °C, 300 °C, 350 °C, and 400 °C) in (a) air atmosphere and (b) nitrogen atmosphere.

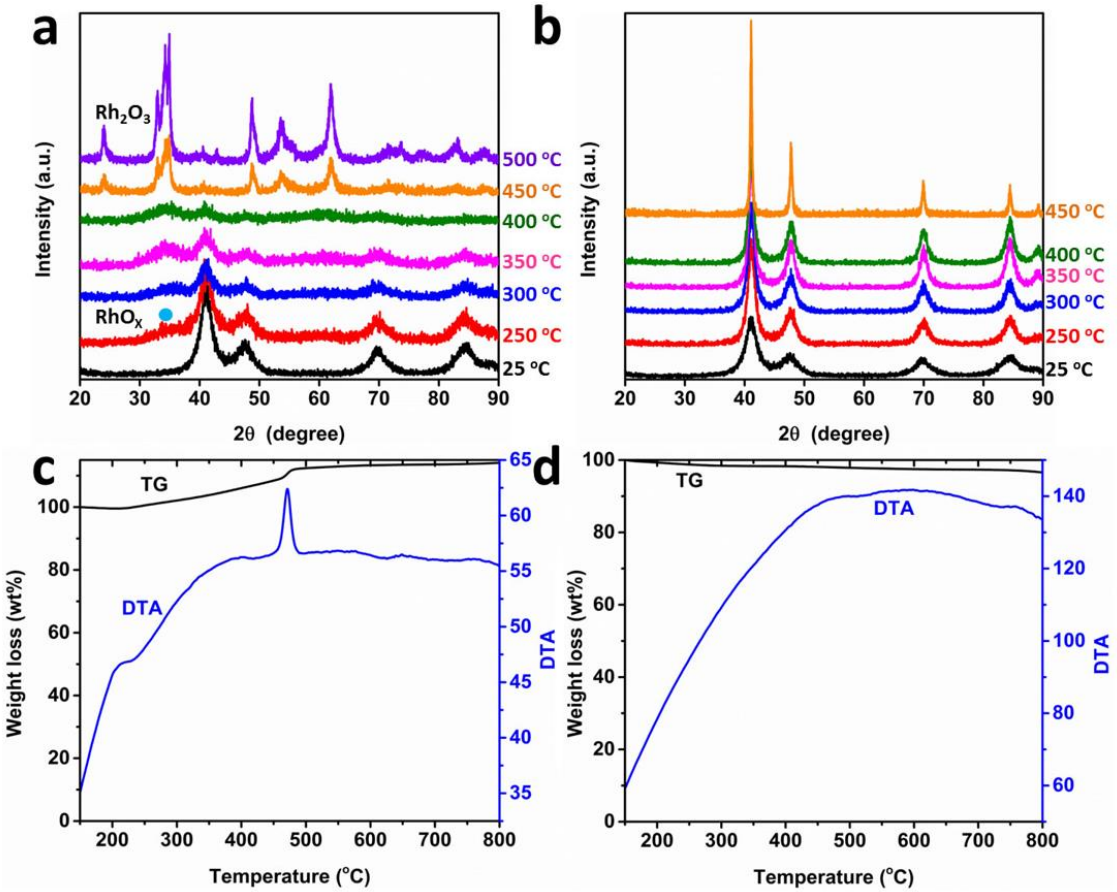


**Supplementary Figure 12. Wide-angle XRD patterns and TG/DTA curves.** Wide-angle XRD patterns of mesoporous Rh nanoparticles after thermal treatment at different temperatures in (a) air atmosphere (25 $^{o}$C, 250 $^{o}$C, 300 $^{o}$C, 350 $^{o}$C, 400 $^{o}$C, 450 $^{o}$C, and 500 $^{o}$C) and (b) nitrogen atmosphere (25 $^{o}$C, 250 $^{o}$C, 300 $^{o}$C, 350 $^{o}$C, 400 $^{o}$C, and 450 $^{o}$C). (c) TG/DTA curves measured in air and (d) TG/DTA curves measured in nitrogen for as-prepared mesoporous Rh nanoparticels. The exothermic peak in panel (c) indicates that Rh is oxidizing somewhat.

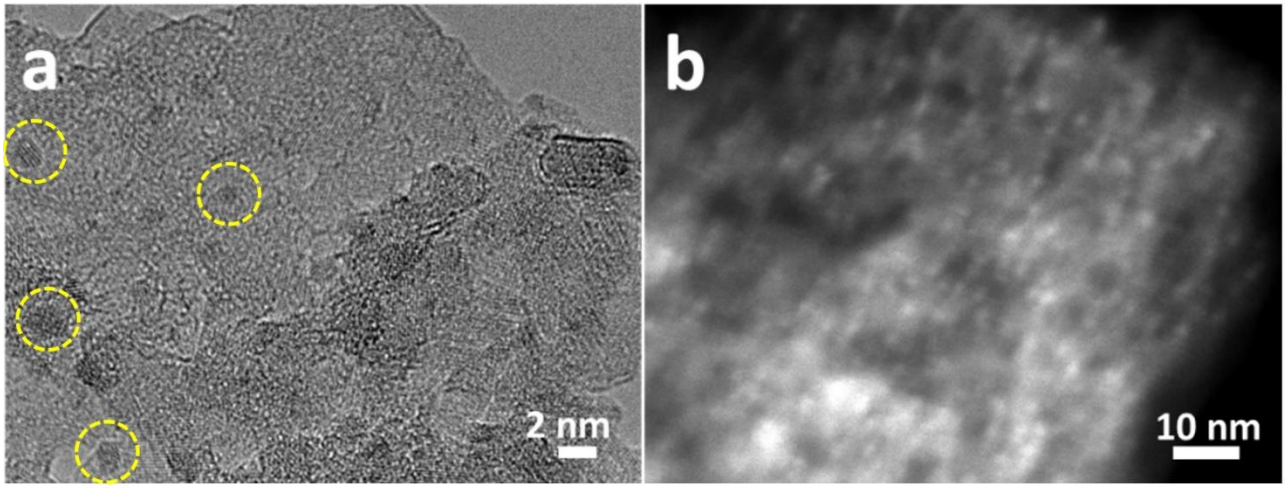


**Supplementary Figure 13. TEM study.** TEM and HAADF-STEM micrographs showing commercially available $Rh/Al_2O_3$. Some of the Rh nanoparticles are highlighted with yellow circles.

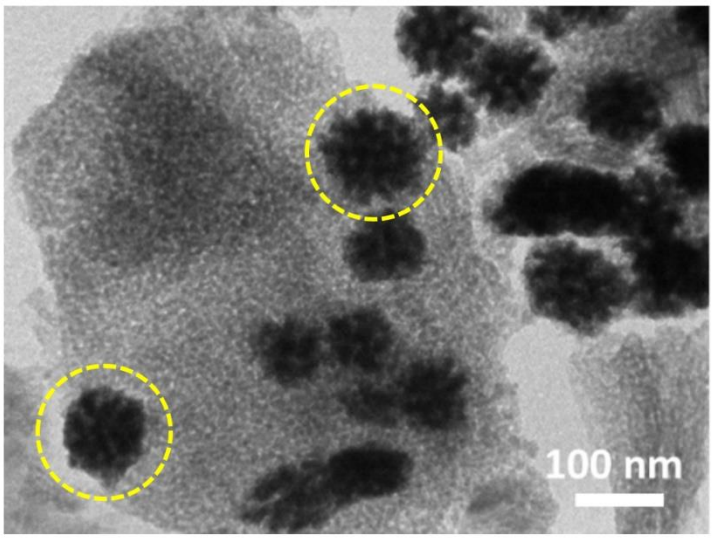


**Supplementary Figure 14. TEM study.** TEM micrograph of mesoporous $Rh/Al_2O_3$. Some mesoporous Rh nanoparticles are highlighted with yellow circles.

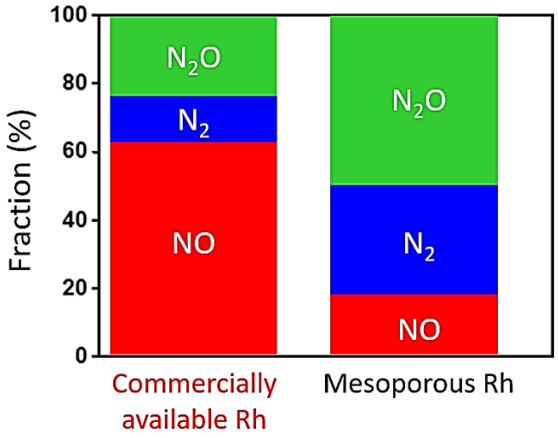


Possible pathways:
(1) $NO + 1/2CO \rightarrow 1/2N_2O + 1/2CO_2$
(2) $NO + CO \rightarrow 1/2N_2 + CO_2$

Selectivity at 250 °C
Commercially available Rh:
$[N_2O]/[N_2]$=2.33 (μmol $min^{-1}$)/1.40 (μmol $min^{-1}$)=1.66

Mesoporous Rh:
$[N_2O]/[N_2]$=4.99 (μmol $min^{-1}$)/3.25 (μmol $min^{-1}$)=1.54

**Supplementary Figure 15. Comparison of the calculated selectivity.** Comparison of the calculated selectivity of mesoporous Rh nanoparticles with commercially available Rh catalysts.

**Supplementary Note 3:** The effluent gas flowing over the mesoporous Rh contains 4.99 μmol $min^{-1}$ of $N_2O$ and 3.25 μmol $min^{-1}$ of $N_2$ at 250 °C, which are generated via different two reaction pathways. The selectivity for the $N_2O$ generation on mesoporous Rh catalyst is calculated as $[N_2O]/[N_2]$ = 4.99 (μmol $min^{-1}$)/3.25 (μmol $min^{-1}$) = 1.54. The alumina-supported Rh catalyst (commercially available Rh) also converted NO to $N_2O$ and/or $N_2$, in which the selectivity for $N_2O$ is calculated as $[N_2O]/[N_2]$ = 2.33 (μmol $min^{-1}$)/1.40 (μmol $min^{-1}$) = 1.66. This simple calculation shows that the commercially available Rh catalyst has similar selectivity for $N_2O$ as the mesoporous Rh catalyst. However, the mesoporous Rh converts NO into $N_2O$ and/or $N_2$ much more efficiently with almost the same selectivity for $N_2O$, resulting in apparently higher $N_2O$ generation. We propose that the mesoporous Rh exhibit high performance due to a combination of high surface area and presence of numerous atomic steps and kink sites which expose unsaturated coordination atoms.

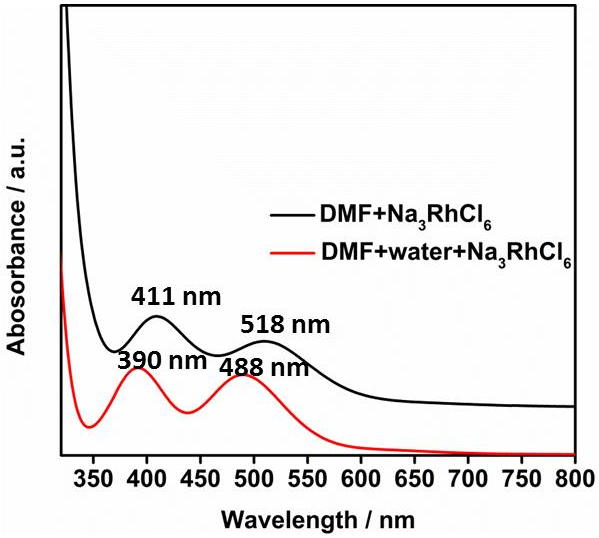


**Supplementary Figure 16. UV-Vis-NIR spectra.** UV-Vis-NIR spectra of DMF+$Na_3RhCl_6$ and DMF+water+$Na_3RhCl_6$, respectively.

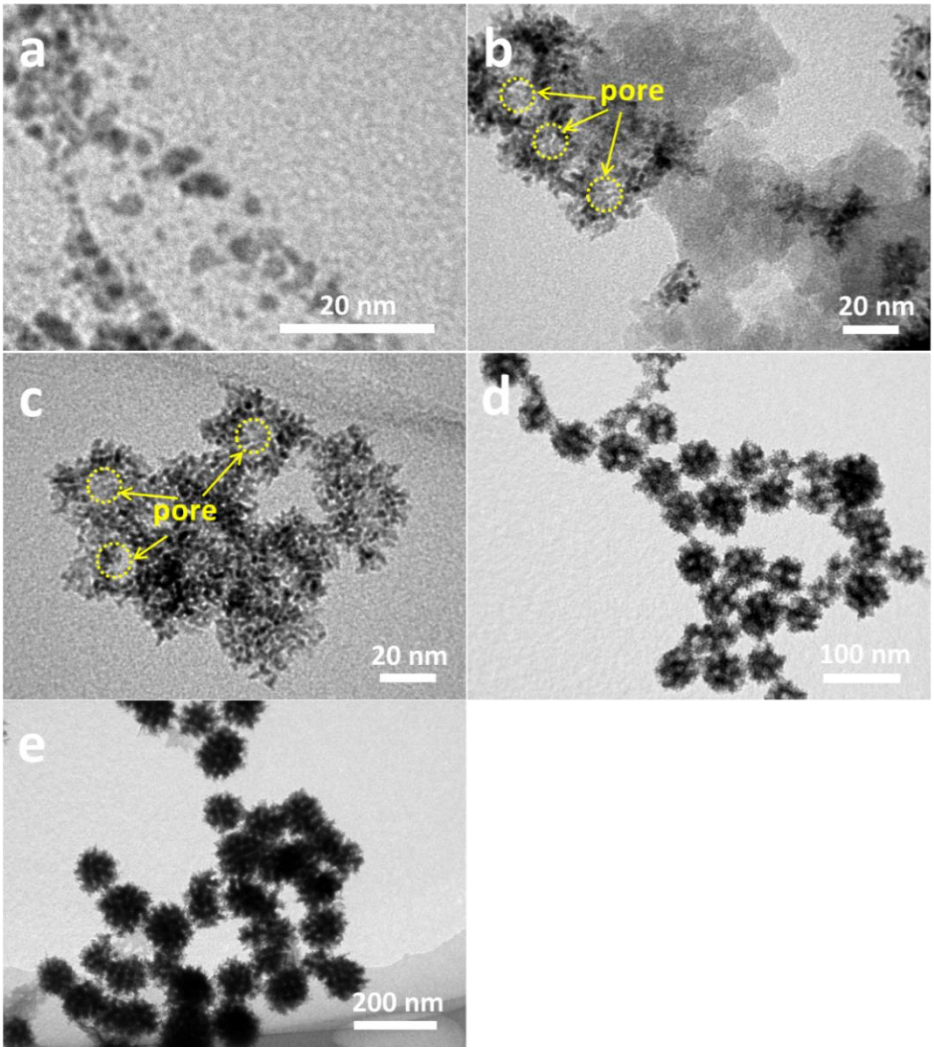


**Supplementary Figure 17. TEM micrographs.** TEM micrographs of Rh samples taken from different reaction periods: (a) 50 min, (b) 60 min, (c) 75 min, (d) 90 min, and (e) 180 min, respectively.

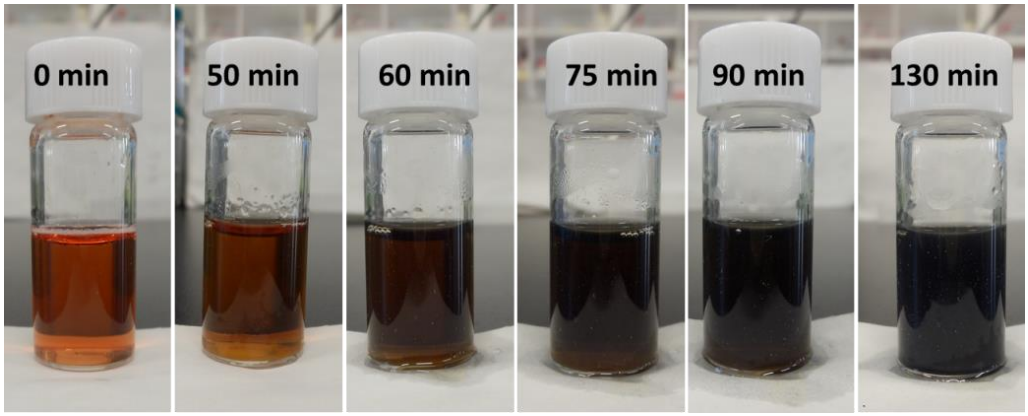


**Supplementary Figure 18. Photographs of colloidal suspensions.** Photographs of colloidal suspensions of reaction solution taken at different reaction times. The reaction was performed at 60 $^{o}$C.

**Supplementary Table 1** Summary on surface areas of mesoporous nanoparticles with various compositions.

| Sample names | Density ($g/cm^3$) | Surface area ($g/m^2$) | Reference |
|---|---|---|---|
| Mesoporous Rh nanoparticles | 12.41 | 50 | Present work |
| Mesoporous $SiO_2$ nanoparticles | 2.65 | 193-500 | 1 |
| Mesoporous $TiO_2$ nanoparticles | 4.23 | 148 | 2 |
| Ordered porous $TiO_2$ | 4.23 | 135 | 3 |
| Mesoporous $In_2O_3$ nanoparticles | 7.18 | 48 | 4 |
| Mesoporous carbon nanoparticles | 1.80-2.10 | 343 | 5 |
| Mesoporous $SnO_2$ | 6.95 | 87 | 6 |

## Supplementary references


[1] Wei, J., Wang, H., Deng, Y., Sun, Z., Shi, L., Tu, B., Luqman, M. Zhao, D. Solvent evaporation induced aggregating assembly approach to three-dimensional ordered mesoporous silica with ultralarge accessible mesopores. *J. Am. Chem. Soc.* **133**, 20369-20377 (2011).

[2] Liu, Y., Lan, K., Li, S., Liu, Y., Kong, B., Wang, G., Zhang, P., Wang, R., He, H., Ling, Y., Al-Enizi, A. M., Elzatahry, A. A., Cao, Y., Chen, G., Zhao D. Constructing three-dimensional mesoporous bouquet-posy-like $TiO_2$ superstructures with radially oriented mesochannels and single-crystal walls. *J. Am. Chem. Soc.* **139**, 517-526 (2017).

[3] Sun, W., Zhou, S., You, B., Wu L. Facile fabrication and high photoelectric properties of hierarchically ordered porous $TiO_2$. *Chem. Mater.* **24,** 3800-3810 (2012).

[4] Ren, Y., Zhou, X., Luo, W., Xu, P., Zhu, Y., Li, X., Cheng, X., Deng, Y., Zhao D. Amphiphilic block copolymer templated synthesis of mesoporous indium oxides with nanosheet-assembled pore walls. *Chem. Mater.* **28**, 7997-8005 (2016).

[5] Tang, J., Liu, J., Li, C., Li, Y., Tade, M. O., Dai, S., Yamauchi, Y. Synthesis of nitrogen-doped mesoporous carbon spheres with extra-large pores through assembly of diblock copolymer micelles. *Angew. Chem. Int. Ed.* **54**, 588-593 (2015).

[6] Wang, X., Li, Z., Li, Q., Wang, C., Chen, A., Zhang, Z., Fan, R., Yin, L. Ordered mesoporous $SnO_2$ with a highly crystalline state as an anode material for lithium ion batteries with enhanced electrochemical performance. *CrystEngComm* **15**, 3696-3704 (2013).